

Article

Multifactorial Model Based on DWI-Radiomics to Determine HPV Status in Oropharyngeal Squamous Cell Carcinoma

Simona Marzi ^{1,*} , Francesca Piludu ², Iliaria Avanzolini ¹, Valerio Muneroni ^{2,3}, Giuseppe Sanguineti ⁴, Alessia Farneti ⁴, Pasqualina D'Urso ⁴, Maria Benevolo ⁵, Francesca Rollo ⁵ , Renato Covello ⁵, Francesco Mazzola ⁶  and Antonello Vidiri ²

¹ Medical Physics Laboratory, IRCCS Regina Elena National Cancer Institute, Via Elio Chianesi 53, 00144 Rome, Italy; ilaria.avanzolini@ifo.it

² Radiology and Diagnostic Imaging Department, IRCCS Regina Elena National Cancer Institute, Via Elio Chianesi 53, 00144 Rome, Italy; francesca.piludu@ifo.it (F.P.); muneronivalerio@gmail.com (V.M.); antonello.vidiri@ifo.it (A.V.)

³ Scuola di Specializzazione in Radiodiagnostica, Sapienza Università di Roma—Policlinico Umberto I, Viale Regina Elena 324, 00161 Rome, Italy

⁴ Department of Radiotherapy, IRCCS Regina Elena National Cancer Institute, Via Elio Chianesi 53, 00144 Rome, Italy; giuseppe.sanguineti@ifo.it (G.S.); alessia.farneti@ifo.it (A.F.); pasqualina.durso@ifo.it (P.D.)

⁵ Pathology Department, IRCCS Regina Elena National Cancer Institute, Via Elio Chianesi 53, 00144 Rome, Italy; maria.benevolo@ifo.it (M.B.); francesca.rollo@ifo.it (F.R.); renato.covello@ifo.it (R.C.)

⁶ Otolaryngology & Head and Neck Surgery, Regina Elena National Cancer Institute, Via Elio Chianesi 53, 00144 Rome, Italy; francesco.mazzola@ifo.it

* Correspondence: simona.marzi@ifo.it



Citation: Marzi, S.; Piludu, F.; Avanzolini, I.; Muneroni, V.; Sanguineti, G.; Farneti, A.; D'Urso, P.; Benevolo, M.; Rollo, F.; Covello, R.; et al. Multifactorial Model Based on DWI-Radiomics to Determine HPV Status in Oropharyngeal Squamous Cell Carcinoma. *Appl. Sci.* **2022**, *12*, 7244. <https://doi.org/10.3390/app12147244>

Academic Editors: Marco Giannelli, Andrea Barucci and Chiara Marzi

Received: 10 June 2022

Accepted: 15 July 2022

Published: 19 July 2022

Publisher's Note: MDPI stays neutral with regard to jurisdictional claims in published maps and institutional affiliations.



Copyright: © 2022 by the authors. Licensee MDPI, Basel, Switzerland. This article is an open access article distributed under the terms and conditions of the Creative Commons Attribution (CC BY) license (<https://creativecommons.org/licenses/by/4.0/>).

Featured Application: Imaging-based predictors of HPV status could be used to non-invasively detect HPV positivity in cases in which biopsy is not feasible because of a hardly accessible tumor location, or when the HPV test results are conflicting. Radiomics signatures for HPV status would also help in OPSCC for an easier diagnosis in unknown primary head and neck tumors, contributing to reducing costs and invasiveness of the current gold-standard modality for disease diagnosis and staging. Lastly, it would be of interest to explore the role of image-based signatures for HPV status classification as prognostic biomarkers, in order to better identify distinct risk classes of OPSCC patients.

Abstract: Background: Oropharyngeal squamous cell carcinoma (OPSCC) associated with human papillomavirus (HPV) has higher rates of locoregional control and a better prognosis than HPV-negative OPSCC. These differences are due to some unique biological characteristics that are also visible through advanced imaging modalities. We investigated the ability of a multifactorial model based on both clinical factors and diffusion-weighted imaging (DWI) to determine the HPV status in OPSCC. Methods: The apparent diffusion coefficient (ADC) and the perfusion-free tissue diffusion coefficient D were derived from DWI, both in the primary tumor (PT) and lymph node (LN). First- and second-order radiomic features were extracted from ADC and D maps. Different families of machine learning (ML) algorithms were trained on our dataset using five-fold cross-validation. Results: A cohort of 144 patients was evaluated retrospectively, which was divided into a training set (n = 95) and a validation set (n = 49). The 50th percentile of D_{PT} , the inverse difference moment of ADCLN, smoke habits, and tumor subsite (tonsil versus base of the tongue) were the most relevant predictors. Conclusions: DWI-based radiomics, together with patient-related parameters, allowed us to obtain good diagnostic accuracies in differentiating HPV-positive from HPV-negative patients. A substantial decrease in predictive power was observed in the validation cohort, underscoring the need for further analyses on a larger sample size.

Keywords: human papillomavirus; oropharyngeal squamous cell carcinoma; magnetic resonance imaging; diffusion magnetic resonance imaging; machine learning; radiomics

1. Introduction

In the last two decades, a growing number of pre-clinical and clinical studies have focused on the biological and molecular mechanisms of HPV-associated oropharyngeal squamous cell carcinoma (OPSCC) in order to explain its peculiar radio- and chemio-responsiveness. These studies identified specific tumor microenvironmental factors and a lower ability of this kind of malignancies to repair DNA damage and to repopulate after radiation-induced injury [1]. The substantially better prognosis of patients with HPV-related OPSCC compared to those with HPV-negative OPSCC has been defined in the American Joint Committee on Cancer TNM8 staging guidelines, which recommend stratification by HPV status to improve staging [2,3].

The diagnosis, staging, and follow-up of OPSCC are highly dependent on imaging [4], including ultrasound, computed tomography (CT), magnetic resonance imaging (MRI), and positron emission tomography (PET). In clinical practice, MRI is often the modality of choice because it is a multiparametric imaging modality that provides morphologic data with high soft-tissue contrast [5]. Furthermore, MRI can investigate the physical properties of the tumor, i.e., the microvascular and cellular architecture of tissues, by the application of additional sequences such as dynamic-contrast-enhanced (DCE-MRI) and diffusion-weighted imaging (DWI), respectively [6].

In recent years, growing attention has also been paid to radiomics, which refers to the automated extraction of mathematically defined radiological features from two- or three-dimensional (2D or 3D) medical images. By converting medical images into high-dimensional, mineable data via high-throughput extraction of quantitative features (e.g., morphology, intensity histogram, and texture), additional information beyond the original raw images can be obtained [7].

The recent application of radiomics in head and neck studies demonstrated promising results to obtain a better diagnosis and a more accurate prediction of tumor response to treatments and of normal tissue toxicity [8–12]. These novel developments in medical imaging are also promoted by a machine learning approach to high-dimensional data analysis and model building, which is continuously updated and improved [7,8].

Multiple studies have already developed CT-based radiomic signatures for predicting HPV status [13–16], while only a few studies focused on MRI-based radiomics, taking advantage of the better soft-tissue contrast of morphological sequences than CT, and of functional information provided by diffusion- and perfusion-weighted techniques [17–19]. The clinical utility of DWI in discriminating HPV-positive from HPV-negative patients and its superiority with respect to morphological sequences, i.e., T2-weighted and/or contrast-enhanced T1-weighted imaging, has been recently suggested by the investigation of Suh et al. [19] and supported by previous correlation studies between DWI and histopathology in HNSCC [20,21]. For these reasons, we hypothesized that DWI-based radiomics could be particularly helpful to non-invasively detect HPV positivity and to better explore the peculiar tissue architecture of HPV-associated OPSCC.

The aim of this study is to investigate, through a radiomic approach, the potential role of DWI in predicting HPV status in patients affected by OPSCC.

2. Materials and Methods

2.1. Patient Population

This cohort study was conducted retrospectively at the IRCCS Regina Elena National Cancer Institute, Rome, Italy. The study was authorized by the hospital ethics committee, i.e., ‘The Central Ethics Committee, IRCCS LAZIO, IFO’ with a reference number RS1701/22.

Inclusion criteria were: (i) pathologically confirmed OPSCC; (ii) no distant metastasis; and (iii) MRI exam including DWI obtained with at least three b values ($b = 0, 500, \text{ and } 800 \text{ s/mm}^2$); (iv) HPV test result. Exclusion criteria were: (i) the presence of artifacts in the DWI that prevent a quantitative evaluation and (ii) prior surgery or chemo-radiotherapy to the primary disease and the neck.

The tumor subsite was determined according to the anatomical site in which the greater part of the tumor is located and based on the routes of the tumor spread. Specifically, the base of the tongue is the posterior third of the tongue extending inferiorly to the valleculae; it can spread to the tonsillar fossa, sublingual space, and into the valleculae. The tonsillar subsites are the anterior and posterior tonsillar pillars and palatine tonsil; the tumor can spread into the base of the tongue, parapharyngeal and masticator spaces, nasopharynx, and skull base. The tumor subsite classification was performed by two HN radiologists in consensus, with more than 20 and 10 years of experience (A.V. and F.P.).

Patients were classified based on smoking habits and alcohol consumption as non-drinkers, moderate alcoholics if they drank <1 L of wine/day and heavy alcoholics if they drank ≥ 1 L of wine/day; non-smokers if they smoked <5 packs/year, moderate smoker if they smoked ≥ 6 packs/year, or heavy smoker if they smoked ≥ 24 packs/year.

2.2. HPV Testing

HPV testing and p16 immunohistochemistry were performed on formalin-fixed paraffin-embedded tissues. HPV-DNA detection and genotyping were performed using the Inno-LiPA HPV Genotyping Extra II kit (Fujirebio, Tokyo, Japan) based on the SPF10 primer set, which allows the detection of 32 HPV genotypes, including those classified as high risk by the International Agency for Research on Cancer. Immunohistochemical staining for the p16 protein was performed using the CINtec[®] Histology kit (Roche Diagnostics, Basel, Switzerland), following the manufacturer's instructions. The immunostaining was referred to as positive when a diffuse nuclear and cytoplasmic expression was observed in more than 75% of tumor cells [2]. OPSCC cases were considered HPV-attributable when they showed positivity for both HPV-DNA and p16 immunostaining [22].

2.3. MRI Acquisition Protocol

All patients underwent MRI scans on a 1.5T system (Optima[™] MR450w, GE Healthcare, Milwaukee, WI, USA) or a 3T system (Discovery MR750w; GE Healthcare, Milwaukee, WI, USA) with 24-channel phased array RF coil. The protocol included T2-weighted images in both coronal and axial planes (field of view, 26–28 cm; acquisition matrix, 288 \times 256; slice thickness, 4 mm).

On the 1.5T system, DWI was obtained using axial echo-planar imaging (EPI) sequences, with diffusion-sensitizing gradients applied in three orthogonal directions to derive trace-weighted images (field of view, 28 cm; TR/TE, 4500/72 ms; acquisition matrix, 128 \times 128, slice thickness, 4 mm; pixel bandwidth 1953 MHz). Multiple b values were used including $b = 0, 500, \text{ and } 800 \text{ s/mm}^2$. Three signal averages for b values of 0 s/mm^2 , four for b values of 500 s/mm^2 , and five for b values of 800 s/mm^2 were chosen, with a scan time reduction factor of 2.

Similarly, on the 3T system, DWI was performed using EPI sequences with three b values, $b = 0, 500, \text{ and } 800 \text{ s/mm}^2$ (field of view, 25 cm; TR/TE 6500/77 ms; acquisition matrix, 160 \times 96; slice thickness, 4 mm; pixel bandwidth 1953 MHz). Four signal averages for b values of 0 s/mm^2 , eight for b values of 500 s/mm^2 , and 16 for b values of 800 s/mm^2 were chosen, with a scan time reduction factor of 2.

Both the conventional ADC and the perfusion-free tissue diffusion coefficient D were derived [23]. ADC was obtained from data at b values of 0, 500, and 800 s/mm^2 , while D was derived from data at b values of 500 and 800 s/mm^2 . The commercial software package Ready View (GE Advantage Workstation, READYView, Palo Alto, CA, USA) was used to automatically generate both ADC and D maps.

2.4. Image and Feature Processing

3D Slicer Software (version 4.11) was used for image visualization and segmentation [24]. Both the primary tumor (PT) and the largest lymph node (LN) were delineated on DWI at $b = 800 \text{ mm}^2/\text{s}$ by two HN radiologists in consensus (A.V. and F.P.), using

T2-weighted images as a guide. Each contour mask was rigidly propagated on both ADC and D maps and saved as a DICOM file.

Diffusion maps and structure set files were imported into S-IBEX software [25] to calculate the radiomic features. It is a standardized version of IBEX (image biomarker explorer) software [26], adapted and validated consistently with the guidelines of the Image Biomarker Standardization Initiative (IBSI) [27].

Eight families of features were extracted from a 3D analysis of both ADC and D maps: Intensity Direct (39 features), Intensity Histogram (13 features), Gray Level Co-occurrence Matrix or GLCM (25 features), Gray Level Distant Zone Matrix (GLDZM) (25 features), Gray Level Run Length Matrix (GLRLM) (16 features), Gray Level Size Zone Matrix (16 features), Neighboring Gray Level Dependence (16 features), and Morphology (16 features), for a total of 157 features for each PT and LN.

A detailed list of the features and the image pre-processing steps (interpolation, re-segmentation, intensity discretization) are reported in Supplemental Tables S1 and S2.

The outliers, i.e., data that were more than three median absolute deviations away from the median, were removed from the value distribution of each feature to improve the reliability of radiomics [28]. To remove the dependency of some features from the lesion volume, the Spearman rank correlation (Rho) test was used and, in case of highly positive or negative correlation ($Rho > 0.85$ or $Rho < -0.85$), their values were normalized for the corresponding PT/LN volume.

The harmonization between 1.5 and 3T systems was performed at the feature level using the ComBat algorithm [29] via the package neuroCombat in R Studio [RStudio Team (2020). RStudio: Integrated Development for R. RStudio, PBC, Boston, MA, USA, URL: <http://www.rstudio.com> (accessed on 22 September 2021)].

2.5. Machine Learning Modelling

Before the feature selection, both the training and validation datasets were standardized using the z-score normalization method as described by Haga et al. [30].

The feature selection was performed using the minimum redundancy maximum relevance (MRMR) algorithm, which finds the best predictors among categorical and continuous variables using the mutual information between them [31].

As in our dataset, there was an unequal distribution between HPV-positive and HPV-negative classes, we applied the synthetic minority oversampling technique for nominal and continuous variables (SMOTE-NC) to address the data imbalance during training [32], via the package RSBID in R Studio.

Different families of ML algorithms were trained on our dataset and compared, including Decision Tree, Linear Discriminant, Logistic Regression, Naive Bayes, Support Vector Machine, K-Nearest Neighbor Classifiers, and Ensemble Classifiers. An iterative optimization process was used to select the most appropriate hyperparameters of each algorithm for the model building. A stratified 5-fold cross-validation was applied to limit overfitting and make the models more generalizable (overfitting in ML refers to the model's ability to provide accurate predictions on the training data, while it does not perform well in the validation dataset).

Accuracy, sensitivity, specificity, and AUC (area under the receiver operating characteristic curve) were used to evaluate the model performance. The bias-corrected and accelerated percentile bootstrap method was applied to estimate the confidence interval for the AUC, using 1000 replicates. The mid-*p*-value McNemar test was applied to compare prediction accuracies between different models. The MATLAB Statistics and Machine Learning Toolbox were used to carry out the ML-based model building.

3. Results

3.1. Patient Population

From December 2011 to December 2021, a total of 147 patients were initially included in the present study. Considering the potential role of the tumor subsite in relation to

the HPV status [33], three patients with tumor subsites poorly represented, i.e., posterior wall ($n = 2$) and soft palate ($n = 1$), were excluded. The final patient cohort consisted of 144 patients, which was divided into a training set of 95 patients and a validation set of 49 patients, with a similar proportion of HPV-negative and HPV-positive patients (30%/70% versus 33%/67%, respectively) and T- and N-stage characteristics. The patient and tumor characteristics of both sets are reported in Tables 1 and 2, respectively. Tumor subsite, smoke, and alcohol intake were significantly different between HPV-positive and HPV-negative OPSCC (Table 1). A strong association between smoke and alcohol intake was found ($p = 0.0005$, from the Chi2 test).

Table 1. Characteristics of patients and tumors in the training set.

Patient and Tumor Characteristics		HPV-Negative (n = 28)	HPV-Positive (n = 67)	<i>p</i> -Value *
		n	n	
Gender	Male	26 (93%)	50 (75%)	0.051
	Female	2 (7%)	17 (25%)	
Age (mean \pm SD)		66.4 \pm 9.3	64.4 \pm 9.3	0.334
Tumor subsite	Tonsil	10 (36%)	42 (63%)	0.023
	Base of the tongue	18 (64%)	25 (37%)	
T-stage	T1	4 (14.3%)	8 (11.9%)	
	T2	5 (17.9%)	24 (35.8%)	
	T3	4 (14.3%)	7 (10.4%)	
	T4	-	28 (41.8%)	
	T4a	15 (53.6%)	-	
N-stage	N0	5 (17.9%)	7 (10.4%)	
	N1	4 (14.3%)	29 (43.3%)	
	N2	5 (17.9%)	28 (41.8%)	
	N3	14 (50%)	3 (4.5%)	
Smoke	No	7 (25%)	33 (49.3%)	0.009
	Moderate	2 (7.1%)	11 (16.4%)	
	Heavy	18 (64.3%)	23 (34.3%)	
	Unknown	1 (3.6%)	-	
Alcohol intake	No	11 (39.3%)	43 (64.2%)	0.001
	Moderate	4 (14.3%)	18 (26.9%)	
	Heavy	11 (39.3%)	5 (7.4%)	
	Unknown	2 (7.1%)	1 (1.5%)	

* *p*-values between continuous variables refer to the Student's *t* test; *p*-values between categorical variables refer to Chi2 or Fisher's exact test, as appropriate. Statistically significant *p*-values are in bold. No *p*-value was reported for T and N-stage, the staging being different between HPV-positive and HPV-negative OPSCC according to the 8th edition of AJCC Cancer Staging Manual [2].

The ADC/D radiomic analysis of PT was not possible in 12 patients (9 in the training set and 3 in the validation set) because the primary tumor was considered too small or the image quality was not adequate for the feature extraction (motion artifacts and/or susceptibility-induced distortions were evident in proximity to the primary tumor, especially at the base of the tongue, but without affecting the LN analysis).

In the training set, the PT and LN median volumes were 8.4 cm³ (95% CI, 6.0–11.8 cm³) and 5.5 cm³ (95% CI, 4.0–7.4 cm³), respectively; while in the validation set, they were 6.3 cm³ (95% CI, 4.6–9.2 cm³) and 9.9 cm³ (95% CI, 4.7–13.3 cm³), respectively. The differences in PT and LN volumes between the training and validation set were not significant ($p = 0.23$ and 0.25, respectively, from the Mann–Whitney test).

Table 2. Characteristics of patients and tumors in the validation set.

Patient and Tumor Characteristics		HPV-Negative (n = 16)	HPV-Positive (n = 33)
		n	n
Gender	Male	14 (88%)	29 (88%)
	Female	2 (12%)	4 (12%)
Age (mean ± SD)		66.3 ± 8.8	61.8 ± 11.5
Tumor subsite	Tonsil	7 (44%)	20 (61%)
	Base of the tongue	9 (56%)	13 (39%)
T-stage	T1	1 (6%)	4 (12%)
	T2	3 (19%)	14 (43%)
	T3	1 (6%)	2 (6%)
	T4	-	13 (39%)
	T4a	11 (69%)	-
N-stage	N0	2 (12.5%)	4 (12.1%)
	N1	2 (12.5%)	16 (48.5%)
	N2	4 (25%)	12 (36.4%)
	N3	8 (50%)	1 (3%)
Smoke	No	2 (12.5%)	24 (72.7%)
	Moderate	3 (18.8%)	3 (9.1%)
	Heavy	9 (56.3%)	5 (15.2%)
	Unknown	2 (12.5%)	1 (3%)
Alcohol intake	No	3 (18.8%)	26 (78.8%)
	Moderate	6 (37.5%)	5 (15.1%)
	Heavy	5 (31.3%)	-
	Unknown	2 (12.5%)	2 (6.1%)

The patients belonging to the training set were all examined on the 1.5T system, while patients belonging to the validation set were in part examined on the 1.5T system (n = 30) and in part on the 3T system (n = 19), thus for this cohort it was applied the ComBat-based feature harmonization to reduce the scanner-related variability (see Supplementary Figure S1).

3.2. Machine Learning Modelling

The pipeline of the data analysis is shown in Figure 1.

Before feature selection, more than two hundred features of both PT and LN were significantly different between HPV-negative and HPV-positive patients, based on the Mann–Whitney test (Supplementary Table S3). These statistical analyses were conducted to infer the relationships between radiomic features and HPV status and facilitate the interpretability of the following ML-driven models.

The results of feature selection on the training set are illustrated in Figure 2, which shows the ranks of the top ten predictors. Four features were dominant over all the others: the 50th percentile of D_{PT} (i.e., the median value), the inverse difference moment of ADC_{LN} (which is a measure of homogeneity from the GLCM family), smoking habits, and tumor subsite (tonsil versus base of the tongue).

Box-and-whisker plots of the 50th percentile of D_{PT} and Inverse Difference Moment of ADC_{LN} , sorted by HPV status, are illustrated in Figure 3; the median (inter-quartile range) of the 50th percentile of D_{PT} was $1.15 \times 10^{-3} \text{ mm}^2/\text{s}$ (0.25) and $0.91 \times 10^{-3} \text{ mm}^2/\text{s}$ (0.24) for HPV-negative and HPV-positive patients, respectively ($p < 0.001$, Mann–Whitney test); analogously, the median (inter-quartile range) of Inverse Difference Moment of ADC_{LN} was 0.30 (0.07) and 0.41 (0.12) for HPV-negative and HPV-positive patients, respectively ($p < 0.001$).

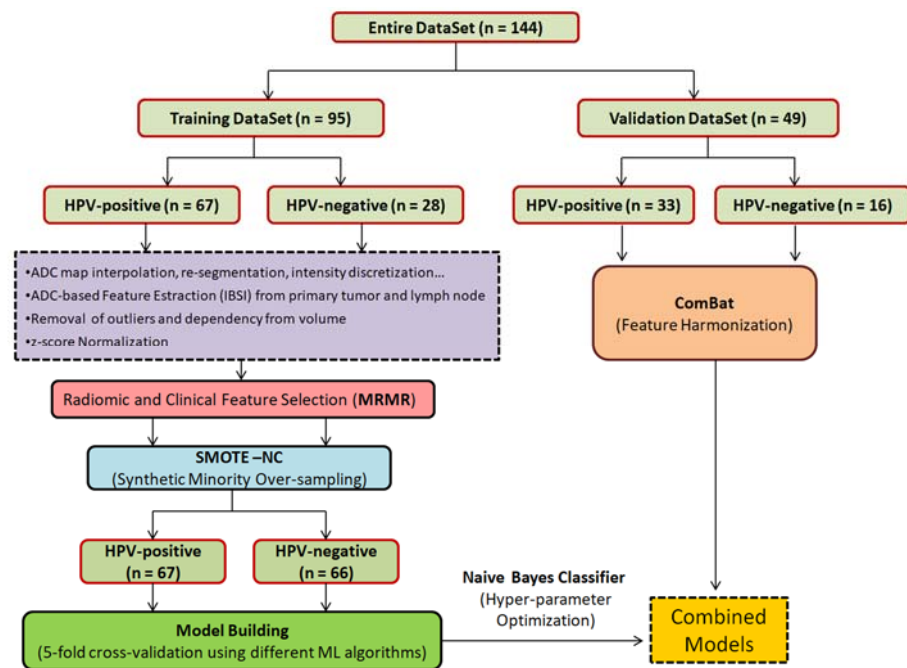


Figure 1. Data analysis pipeline.

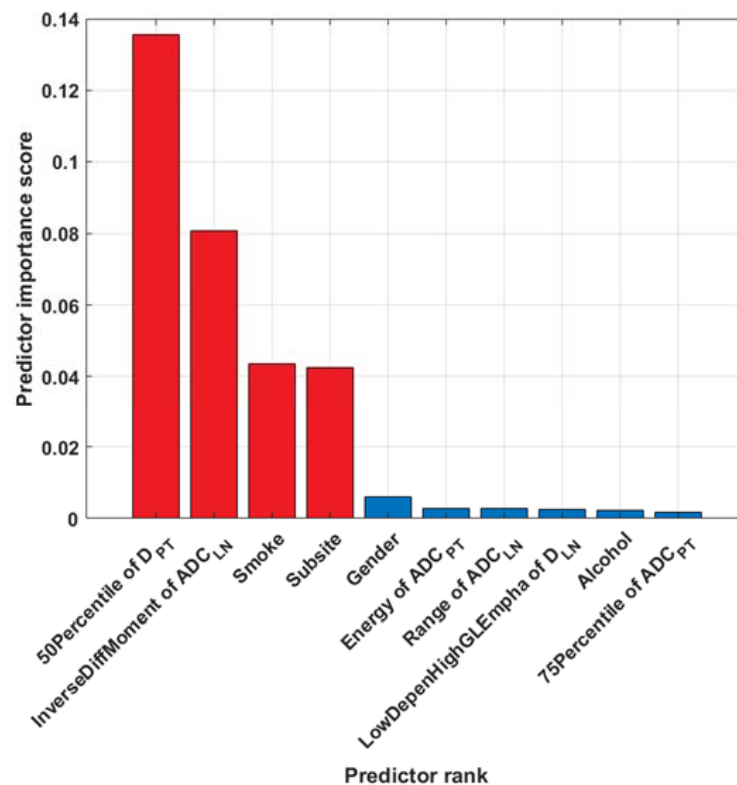


Figure 2. Selection of the most relevant features and the corresponding predictor ranks obtained from the Minimum Redundancy Maximum Relevance (MRMR) algorithm.

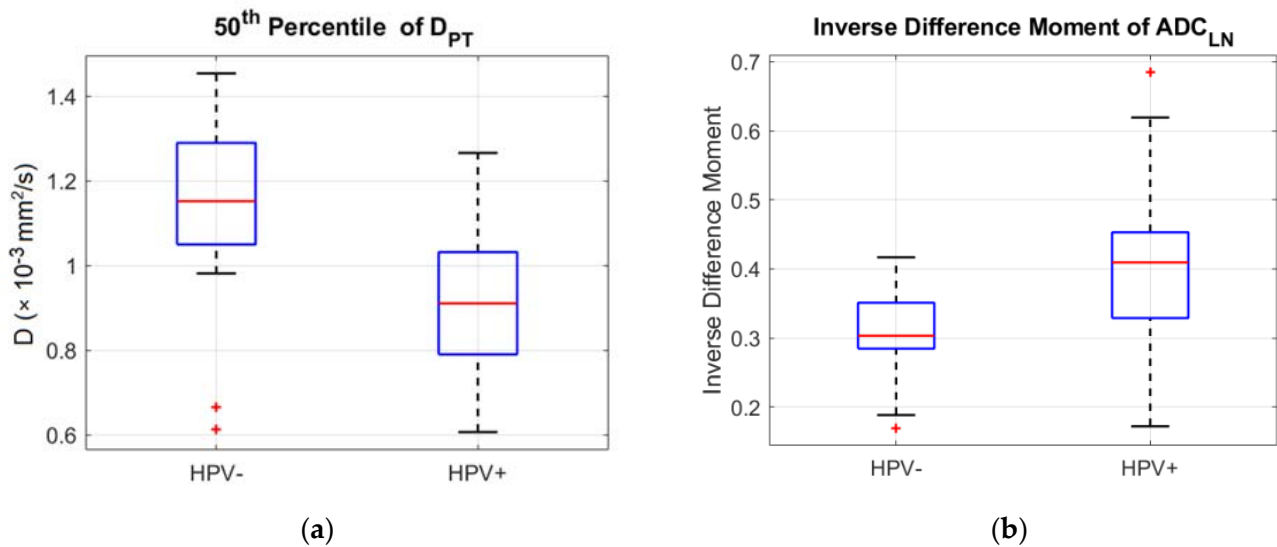


Figure 3. Box-and whisker plot of 50th percentile of D_{PT} (a) and Inverse Difference Moment of ADC_{LN} (b) sorted by HPV status.

Among the different families of ML algorithms, which were trained on the first ten predictors, the Naive Bayes classifier provided the best results in terms of accuracy, as depicted in Supplementary Figure S2. Therefore, we explored the model performance by various combinations of the most relevant predictors using the Naive Bayes algorithm.

We applied the SMOTE-NC technique during training after the feature selection, in order to reduce the number of variables and thus the impact of missing values and sparse data on the random oversampling. In fact, the SMOTE-NC algorithm does not work with NA (not available) values; NA values were due to both the intrinsic nature of data, really missing values or post-processing effects (i.e., some patients did not have LN ADC/D data because they were classified as N0, or some missing values were a consequence of the outlier removal).

The results of the training and validation set are reported in Table 3. No statistically significant differences were found between the models tested on the validation cohort (Supplementary Table S4).

Table 3. Predictive performance of the proposed models on the training cohort and validation cohort (in bold).

Model	Selected Features	Accuracy (%)	Sensitivity (%)	Specificity (%)	AUC
1	50th Percentile of D_{PT} , Inverse Difference Moment of ADC_{LN} , Smoke, Subsite, Gender, Energy of ADC_{PT}	92 [86, 96]	91 [82, 97]	94 [85, 98]	0.95 [0.89, 0.97]
		67 [52, 80]	73 [54, 87]	56 [30, 80]	0.67 [0.45, 0.83]
2	50th Percentile of D_{PT} , Inverse Difference Moment of ADC_{LN} , Smoke, Subsite, Gender	89 [82, 94]	88 [78, 95]	91 [81, 97]	0.95 [0.88, 0.98]
		67 [52, 80]	76 [58, 89]	50 [25, 75]	0.81 [0.62, 0.92]
3	50th Percentile of D_{PT} , Inverse Difference Moment of ADC_{LN} , Smoke, Subsite	88 [81, 93]	87 [76, 94]	91 [81, 97]	0.94 [0.88, 0.97]
		69 [56, 82]	79 [61, 91]	50 [25, 75]	0.78 [0.60, 0.90]
4	50th Percentile of D_{PT} , Inverse Difference Moment of ADC_{LN} , Smoke	86 [79, 91]	85 [74, 93]	88 [78, 95]	0.92 [0.86, 0.96]
		73 [59, 85]	85 [68, 95]	50 [25, 75]	0.79 [0.62, 0.90]
5	50th Percentile of D_{PT} , Inverse Difference Moment of ADC_{LN}	82 [75, 88]	79 [67, 88]	89 [79, 96]	0.91 [0.84, 0.95]
		67 [52, 80]	70 [51, 84]	63 [35, 85]	0.66 [0.51, 0.80]
6	Smoke, Subsite, Gender, Alcohol	85 [78, 90]	90 [80, 96]	76 [63, 85]	0.87 [0.79, 0.92]
		80 [66, 90]	94 [80, 99]	50 [25, 75]	0.82 [0.64, 0.93]

Some representative cases of patients correctly and incorrectly classified are illustrated in Figures 4 and 5.

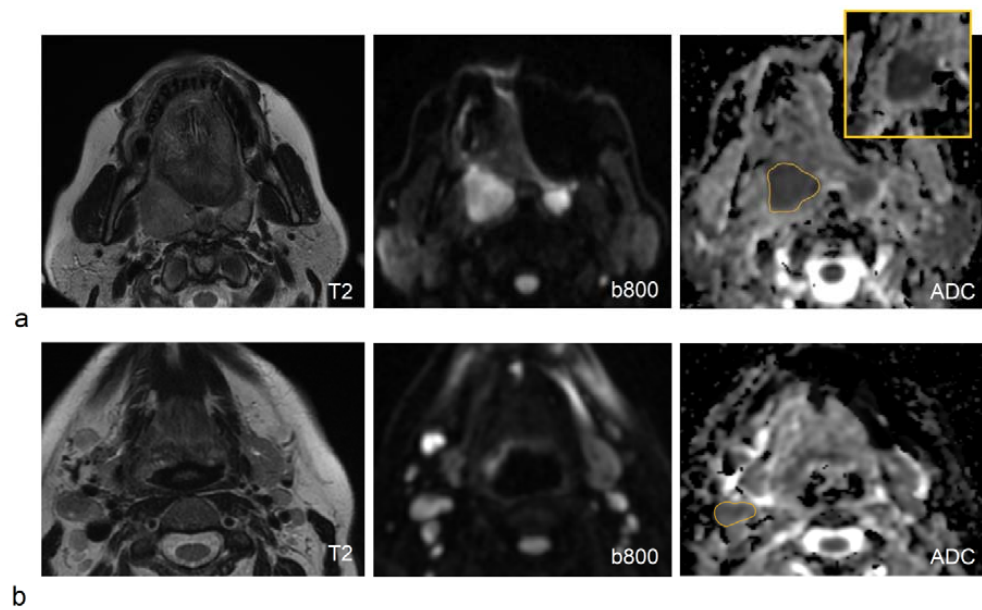


Figure 4. HPV-positive OPSCC in a 57-year-old non-smoker non-alcoholic female, correctly classified by all the proposed models. MRI shows a lesion in the right palatine tonsil, characterized by a homogeneous and moderate signal intensity on the T2-weighted image and a hyperintense signal on DWI obtained with $b = 800$ s/mm². Consistently, both ADC and D maps (the latter was cropped in the upper right yellow box) indicate strongly decreased values in the user-defined lesion contour (yellow line), with 50th percentiles of 0.87×10^{-3} mm²/s and 0.76×10^{-3} mm²/s, respectively (a). Bottom: the same patient had a pathological lymph node at the right IIa level, showing a homogeneous signal intensity on the T2-weighted image, a mildly hyperintense signal on the DWI obtained with $b = 800$ s/mm², and intermediate and uniform values on the ADC map (yellow line), with an Inverse Difference Moment of ADC_{LN} equal to 0.46 (b).

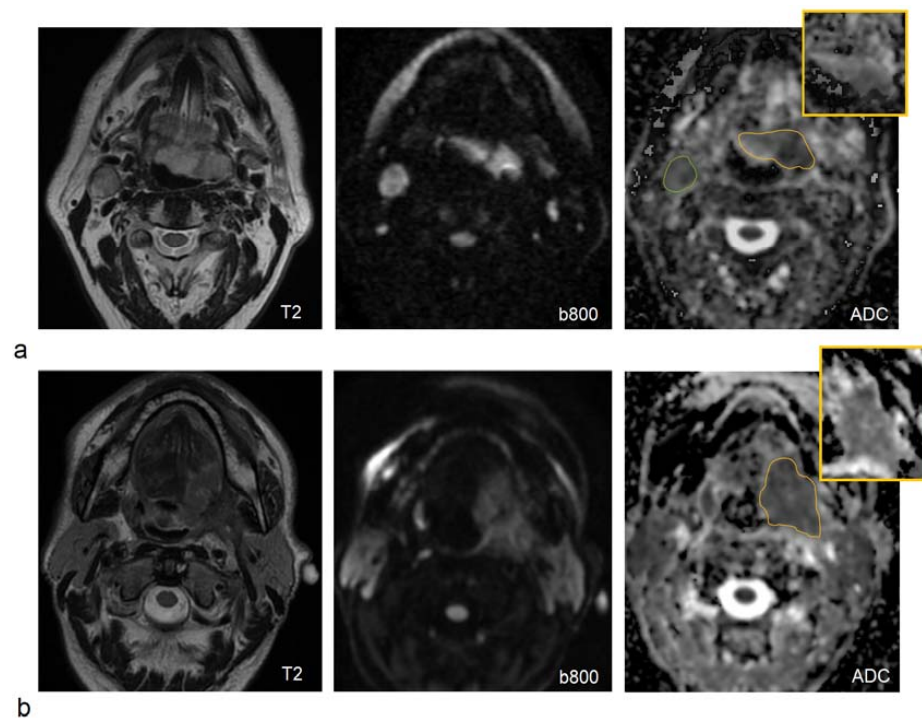


Figure 5. HPV-negative OPSCC in a 72-year-old non-smoker non-alcoholic male. MRI shows a lesion into the base of the tongue with floor of the mouth involvement, characterized by a hyperintense signal

on both T2-weighted image and DWI obtained with $b = 800 \text{ s/mm}^2$. ADC and D maps (the latter was cropped in the upper right yellow box) indicate slightly decreased values in the user-defined primary tumor contour (yellow line), with 50th percentiles of $1.52 \times 10^{-3} \text{ mm}^2/\text{s}$ and $1.29 \times 10^{-3} \text{ mm}^2/\text{s}$, respectively. The pathological lymph node into the IIa level (green line) shows a quite homogeneous signal intensity on the T2-weighted image and rather inhomogeneous signal intensity on DWI, consistent with a low Inverse Difference Moment of ADC_{LN} of 0.28 (a). These patients were correctly classified as HPV-negative by imaging-based or combined models (Model 1-Model 6) but incorrectly classified as HPV-positive by the clinical model (Model 7), smoke and drinking habits being peculiar to a patient affected by an HPV-related malignancy. Bottom: HPV-positive OPSCC in a 67-year-old heavy smoker and alcoholic male. MRI shows a lesion into the base of the tongue, with left palatine tonsil involvement, characterized by a quite homogeneous and moderate hyperintense signal on T2-weighted image and DWI (b). ADC and D maps indicate moderately decreased values in the user-defined primary tumor contour (yellow line), with the 50th percentile equal to $1.33 \times 10^{-3} \text{ mm}^2/\text{s}$ and $1.12 \times 10^{-3} \text{ mm}^2/\text{s}$, respectively. This patient was misclassified by all the proposed models, having smoke/drinking habits and ADC/D characteristics more indicative of an HPV-negative tumor.

4. Discussion

In the present investigation, we explored the potential of DWI-based radiomics of both primary tumors and metastatic nodes, in conjunction with patient-related factors, to determine the patient HPV status in a homogeneous cohort of OPSCCs.

The role of DWI in differentiating HPV-positive from HPV-negative patients was concordantly reported in previous studies, which found a marked reduction in ADC values and a more leptokurtic and skewed right ADC histogram in HPV-positive tumors, compared to HPV-negative tumors [18,34–37]. This was attributed to the peculiar tissue architecture of HPV-positive tumors, characterized by more densely packed cells, a smaller tumor-stroma component, and higher levels of tumor-infiltrating lymphocytes.

Although more than 200 features extracted from both PTs and LNs were significantly related to HPV status in our training set, only two of them were selected as the best predictors from the MRMR algorithm: the 50th percentile of D_{PT} and the inverse difference moment of ADC_{LN} (which represents an index of homogeneity from GLCM family), together with smoke habits and tumor subsite.

The selection of the 50th percentile of D_{PT} in place of the 50th percentile of ADC_{PT} (even though strongly correlated with HPV status as well) seemed to confirm that the perfusion-free diffusion coefficient, D , may better reveal the specific HPV-positive tumor characteristics related to cell density and tissue microstructure, compared to ADC, as also supported by other investigators [36,38]. The increase in inverse difference moment of ADC in HPV-positive patients indicated a higher homogeneity of metastatic lymph nodes, in accordance with a number of previous studies based on both CT and PET imaging, which reported an increase in homogeneity of CT density and in FDG uptakes [13–16,39]. This can be explained considering the different mechanisms of carcinogenesis between HPV-positive and HPV-negative HNSCCs, the former being more homogeneously triggered by the HPV infection, the latter being the consequence of more intricate genetic alterations attributable to the toxic effect of alcohol drinking and tobacco smoking [12,33].

The important role of both smoking habits and alcohol consumption consistently emerged also from our findings, indicating that patients with HPV-negative OPSCC smoked and drank more than patients with HPV-related OPSCC [33–36]. The quite large patient population included in the present study allowed us to identify the potential of the tumor subsite in distinguishing HPV-positive from -negative subjects, which was scarcely documented in earlier studies. In accordance with Bos et al. [33], OPSCCs located in the tonsil were found to have an increased risk of HPV positivity with respect to those in the base of the tongue.

The entire patient cohort of 144 subjects was split into a training set and a validation set to test the possibility of generalizing and transporting the proposed models to a completely

separate patient group, according to the TRIPOD (Transparent Reporting of a multivariable prediction model for Individual Prognosis or Diagnosis) statements [40].

As several ML algorithms can be used to guide the model building, each of which offers specific advantages and disadvantages in terms of interpretability, assumptions about the data, and computational performance, we trained different families of ML algorithms, identifying the Naive Bayes method as the best classifier in terms of diagnostic accuracy. The main benefits of Naive Bayes algorithms are the simplicity and robustness to missing and noisy data, and the ability to work well also on small sample sizes [7].

To better explore the role of imaging and clinical predictors, alone or in combination, we proposed six possible models, including 50th Percentile of D_{PT} , Inverse Difference Moment of ADC_{LN} , Smoke, Subsite, Gender, and Energy of ADC_{PT} . The maximum number of predictors was limited to six to reduce overfitting in consideration of the size of the training set and the dramatic reduction of the predictor ranks already after the first four features. In the training set, all models provided fair to good accuracies (ranging between 82% and 92%), with high sensitivities (ranging between 79% and 91%), and specificities (ranging between 76% and 94%).

A substantial decrease in diagnostic performances was found after testing the models on the validation cohort: the decrease in accuracy (ranging between 67% and 80%) can be mainly attributable to a marked reduction in specificity (ranging between 50% and 63%), while the sensitivity remained still high or was further improved (73–94%).

The models tested on the validation cohort also suggested superiority of the clinical model (Model 6) in terms of sensitivity, while a slight superiority of combined or image-based models in terms of specificity, although no significant differences emerged. It can also be noted that simpler models, i.e., those including a smaller number of predictors, gave a better performance with respect to more complex ones. This may be explained by a reduced overfitting effect of simpler models, which positively impacted the model's transportability on new data.

Although HPV-specific testing is recommended, imaging-based predictors of HPV status could be used to non-invasively detect HPV positivity in cases in which biopsy is not feasible because of a hardly accessible tumor location, or when the HPV test results are conflicting. Radiomics signatures for HPV status would also help in OPSCC for an easier diagnosis in unknown primary head and neck tumors, contributing to reducing costs and invasiveness of the current gold-standard modality for disease staging. Lastly, it would be of interest to explore the role of image-based signatures for HPV status classification as prognostic biomarkers, in order to better identify distinct risk classes of OPSCC patients, as suggested by Leijenaar et al. [14].

This study had some limitations. A larger dataset is needed to further investigate the generalization of our results in an independent cohort. We applied a correction for the class imbalance, HPV-negative patients representing the minority class according to the current prevalence of HPV positivity in OPSCC [41]; however, random oversampling may have also increased the overfitting and decreased the classifier performance on the validation dataset as a final result. It should also be underlined that the proposed models were based on ADC and D quantifications from both PTs and LNs; thus patients with only one representative volume, PT or LN, may have a higher probability of being wrongly classified. In future investigations, we could propose predictive models from DWI-based radiomics of PTs and LNs separately, considered as distinct tumor entities, also in view of their different responses to radio-chemotherapy. It should be noted that, after the process of feature selection, the MRMR algorithm assigned a much higher importance score to the smoke compared to alcohol, although they were both significantly related to HPV status. This may be explained considering the strong association between these factors, thus the algorithm preferred one of them to reduce data redundancy. This result cannot be generalized and may be dependent on the smoking and drinking habits of our patient population. Finally, we could not investigate the role of HPV vaccination as a predictor of HPV status because both the training and the validation cohorts of patients were unvaccinated against HPV.

5. Conclusions

DWI-based radiomics, together with the patient- and tumor-related factors, allowed us to obtain good diagnostic accuracies in differentiating HPV-positive from HPV-negative patients. A substantial decrease in predictive power was observed in the validation cohort, underscoring the need for further analyses on a larger sample size.

Supplementary Materials: The following are available online at <https://www.mdpi.com/article/10.3390/app12147244/s1>, Table S1: List of radiomic features derived from ADC and D maps, Table S2: Details about image pre-processing before feature extraction, Table S3: Values of the most significant features for differentiating HPV-negative from HPV-positive patients, based on the Mann–Whitney test, Table S4: Comparison between the models in the validation set by the mid-p-value McNemar test, Figure S1: The effect of the ComBat-based feature harmonization on the validation set, Figure S2: Comparison between accuracies obtained from different families of machine learning algorithms.

Author Contributions: Conceptualization, S.M. and A.V.; Data curation, V.M., A.F., P.D. and F.M.; Formal analysis, S.M., I.A., M.B., F.R. and R.C.; Funding acquisition, G.S.; Investigation, F.P., A.F. and P.D.; Methodology, S.M. and M.B.; Resources, G.S. and F.R.; Software, F.P., I.A., V.M. and F.M.; Validation, S.M.; Writing—original draft, S.M., F.P. and A.V.; Supervision, A.V. All authors have read and agreed to the published version of the manuscript.

Funding: This research was partially funded by the Italian Association for Cancer Research (AIRC, project No. 23187).

Institutional Review Board Statement: This study was authorized by the hospital ethics committee, i.e., ‘Central Ethics Committee, IRCCS LAZIO, IFO’ with the reference number RS1701/22.

Informed Consent Statement: Patient consent was waived due to the retrospective nature of the study.

Data Availability Statement: The original contributions presented in the study are included in the article/supplementary material. Further inquiries can be directed to the corresponding author.

Conflicts of Interest: The authors declare no conflict of interest. The funders had no role in the design of the study; in the collection, analyses, or interpretation of data; in the writing of the manuscript; or in the decision to publish the results.

References

1. Spiotto, M.T.; Taniguchi, C.M.; Klopp, A.H.; Colbert, L.E.; Lin, S.H.; Wang, L.; Frederick, M.J.; Osman, A.A.; Pickering, C.R.; Frank, S.J. Biology of the Radio- and Chemo-Responsiveness in HPV Malignancies. *Semin. Radiat. Oncol.* **2021**, *31*, 274–285. [\[CrossRef\]](#)
2. O’Sullivan, B.; Lydiatt, W.M.; Haughey, B.H.; Brandwein-Gensler, M.; Glastonbury, C.M.; Shah, J.P.; Amin, M.B.; Edge, S.; Greene, F. HPV-mediated (p16+) oropharyngeal cancer. In *AJCC Cancer Staging Manual*, 8th ed.; Springer: New York, NY, USA, 2017; pp. 113–121.
3. Craig, S.G.; Anderson, L.A.; Schache, A.G.; Moran, A.G.; Graham, L.; Currie, K.; Rooney, K.; Robinso, M.; Upile, N.S.; Brooker, R.; et al. Recommendations for determining HPV status in patients with oropharyngeal cancers under TNM8 guidelines: A two-tier approach. *Br. J. Cancer* **2019**, *120*, 827–833. [\[CrossRef\]](#)
4. Parvathaneni, U.; Lavertu, P.; Gibson, M.K.; Glastonbury, C.M. Advances in Diagnosis and Multi-disciplinary Management of Oro-pharyngeal Squamous Cell Carcinoma. *State Art. Radiogr.* **2019**, *39*, 2055–2068. [\[CrossRef\]](#)
5. Vishwanath, V.; Jafarieh, S.; Rembielak, A. Imaging at Diagnosis Impacts Cancer Specific Survival of Patients with Cancer of the Oropharynx. *Cancer* **2019**, *125*, 2794–2802.
6. Jansen, J.F.A.; Parra, C.; Lu, Y.; Shukla-Dave, A. Evaluation of head and neck tumors with functional MR imaging. *Magn. Reson. Imaging. Clin. N. Am.* **2016**, *24*, 123–133. [\[CrossRef\]](#)
7. Erickson, B.J.; Korfiatis, P.; Akkus, Z.; Kline, T.L. Machine Learning for Medical Imaging. *Radiographics* **2017**, *37*, 505–515. [\[CrossRef\]](#)
8. Giraud, P.; Giraud, P.; Gasnier, A.; El Ayachy, R.; Kreps, S.; Foy, J.P.; Durdax, C.; Huguet, F.; Burgun, A.; Bibault, J.E. Radiomics and Machine Learning for Radiotherapy in Head and Neck Cancers. *Front. Oncol.* **2019**, *9*, 174. [\[CrossRef\]](#)
9. Yuan, Y.; Ren, J.; Shi, Y.; Tao, X. MRI-based radiomic signature as predictive marker for patients with head and neck squamous cell carcinoma. *Eur. J. Radiol.* **2019**, *117*, 193–198. [\[CrossRef\]](#)
10. Haider, S.P.; Mahajan, A.; Zeevi, T.; Baumeister, P.; Reichel, C.; Sharaf, K.; Forghani, R.; Kucukaya, A.S.; Kann, B.H.; Judson, B.L.; et al. PET/CT radiomics signature of human papilloma virus association in oropharyngeal squamous cell carcinoma. *Eur. J. Nucl. Med. Mol. Imaging* **2020**, *47*, 2978–2991. [\[CrossRef\]](#)

11. Tanadini-Lang, S.; Balermipas, P.; Guckenberger, M.; Pavic, M.; Riesterer, O.; Vuong, D.; Bogowicz, M. Radiomic biomarkers for head and neck squamous cell carcinoma. *Strahlenther. Onkol.* **2020**, *196*, 868–878. [[CrossRef](#)]
12. Salzillo, T.C.; Taku, N.; Wahid, K.A.; McDonald, B.A.; Wang, J.; van Dijk, L.V.; Rigert, J.M.; Mohamed, A.S.R.; Wang, J.; Lai, S.Y.; et al. Advances in Imaging for HPV-Related Oropharyngeal Cancer: Applications to Radiation Oncology. *Semin. Radiat. Oncol.* **2021**, *31*, 371–388. [[CrossRef](#)]
13. Yu, K.; Zhang, Y.; Yu, Y.; Huang, C.; Liu, R.; Li, T.; Yang, L.; Morris, J.S.; Baladandayuthapani, V.; Zhu, H. Radiomic analysis in prediction of Human Papilloma Virus status. *Clin. Transl. Radiat. Oncol.* **2017**, *7*, 49–54. [[CrossRef](#)]
14. Leijenaar, R.T.; Bogowicz, M.; Jochems, A.; Hoebbers, F.J.; Wesseling, F.W.; Huang, S.H.; Chan, B.; Waldron, J.N.; O’Sullivan, B.; Rietveld, D.; et al. Development and validation of a radiomic signature to predict HPV (p16) status from standard CT imaging: A multicenter study. *Br. J. Radiol.* **2018**, *91*, 20170498. [[CrossRef](#)]
15. Bagher-Ebadian, H.; Lu, M.; Siddiqui, F.; Ghanem, A.I.; Wen, N.; Wu, Q.; Liu, C.; Movsas, B.; Chetty, I.J. Application of radiomics for the prediction of HPV status for patients with head and neck cancers. *Med. Phys.* **2020**, *47*, 563–575. [[CrossRef](#)]
16. Song, B.; Yang, K.; Garneau, J.; Lu, C.; Li, L.; Lee, J.; Stock, S.; Braman, N.M.; Koyuncu, C.F.; Toro, P.; et al. Radiomic Features Associated With HPV Status on Pretreatment Computed Tomography in Oropharyngeal Squamous Cell Carcinoma Inform Clinical Prognosis. *Front. Oncol.* **2021**, *11*, 744250. [[CrossRef](#)]
17. Schouten, C.S.; de Graaf, P.; Bloemena, E.; Witte, B.I.; Braakhuis, B.J.; Brakenhoff, R.H.; Leemans, C.R.; Castelijns, J.A.; de Bree, R. Quantitative diffusion-weighted MRI parameters and human papillomavirus status in oropharyngeal squamous cell carcinoma. *AJNR. Am. J. Neuroradiol.* **2015**, *36*, 763–767. [[CrossRef](#)]
18. Nakahira, M.; Saito, N.; Yamaguchi, H.; Kuba, K.; Sugasawa, M. Use of quantitative diffusion-weighted magnetic resonance imaging to predict human papilloma virus status in patients with oropharyngeal squamous cell carcinoma. *Eur. Arch. Otorhinolaryngol.* **2014**, *271*, 1219–1225. [[CrossRef](#)]
19. Suh, C.H.; Lee, K.H.; Choi, Y.J.; Chung, S.R.; Baek, J.H.; Lee, J.H.; Yun, J.; Ham, S.; Kim, N. Oropharyngeal squamous cell carcinoma: Radiomic machine-learning classifiers from multiparametric MR images for determination of HPV infection status. *Sci. Rep.* **2020**, *10*, 17525. [[CrossRef](#)]
20. Driessen, J.P.; van Bommel, A.J.; van Kempen, P.M.; Janssen, L.M.; Terhaard, C.H.; Pameijer, F.A.; Willems, S.M.; Stegeman, I.; Grolman, W.; Philippens, M.E. Correlation of human papillomavirus status with apparent diffusion coefficient of diffusion-weighted MRI in head and neck squamous cell carcinomas. *Head Neck.* **2016**, *38* (Suppl. 1), E613–E618. [[CrossRef](#)]
21. Ward, M.J.; Thirdborough, S.M.; Mellows, T.; Riley, C.; Harris, S.; Suchak, K.; Webb, A.; Hampton, C.; Patel, N.N.; Randall, C.J.; et al. Tumour-infiltrating lymphocytes predict for outcome in HPV-positive oropharyngeal cancer. *Br. J. Cancer.* **2014**, *110*, 489–500. [[CrossRef](#)]
22. Mena, M.; Taberna, M.; Tous, S.; Marquez, S.; Clavero, O.; Quiros, B.; Lloveras, B.; Alejo, M.; Leon, X.; Quer, M.; et al. Double Positivity for HPV-DNA/p16(Ink4a) is the Biomarker with Strongest Diagnostic Accuracy and Prognostic Value for Human Papillomavirus Related Oropharyngeal Cancer Patients. *Oral. Oncol.* **2018**, *78*, 137–144. [[CrossRef](#)]
23. Le Bihan, D.; Breton, E.; Lallemand, D.; Aubin, M.L.; Vignaud, J.; Laval-Jeantet, M. Separation of diffusion and perfusion in intravoxel incoherent motion MR imaging. *Radiology* **1988**, *168*, 497–505. [[CrossRef](#)]
24. Fedorov, A.; Beichel, R.; Kalpathy-Cramer, J.; Finet, J.; Fillion-Robin, J.C.; Pujol, S.; Bauer, C.; Jennings, D.; Fennessy, F.; Sonka, M.; et al. 3D Slicer as an image computing platform for the Quantitative Imaging Network. *Magn. Reson. Imaging.* **2012**, *30*, 1323–1341. [[CrossRef](#)]
25. Bettinelli, A.; Branchini, M.; De Monte, F.; Scaggion, A.; Paiusco, M. Technical Note: An IBEX adaption toward image biomarker standardization. *Med. Phys.* **2020**, *47*, 1167–1173. [[CrossRef](#)]
26. Zhang, L.; Fried, D.V.; Fave, X.J.; Hunter, L.A.; Yang, J.; Court, L.E. Ibex: An open infrastructure software platform to facilitate collaborative work in radiomics. *Med. Phys.* **2015**, *42*, 1341–1353. [[CrossRef](#)]
27. Zwanenburg, A.; Leger, S.; Vallières, M.; Löck, S. Image biomarker standardisation initiative. *arXiv* **2020**, arXiv:1612.07003.
28. Park, B.W.; Kim, J.K.; Heo, C.; Park, K.J. Reliability of CT radiomic features reflecting tumour heterogeneity according to image quality and image processing parameters. *Sci. Rep.* **2020**, *10*, 3852. [[CrossRef](#)]
29. Fortin, J.P.; Parker, D.; Tunç, B.; Watanabe, T.; Elliott, M.A.; Ruparel, K.; Roalf, D.R.; Satterthwaite, T.D.; Gur, R.C.; Gur, R.E.; et al. Harmonization of multi-site diffusion tensor imaging data. *Neuroimage* **2017**, *161*, 149–170. [[CrossRef](#)]
30. Haga, A.; Takahashi, W.; Aoki, S.; Nawa, K.; Yamashita, H.; Abe, O.; Nakagawa, K. Standardization of imaging features for radiomics analysis. *J. Med. Investig.* **2019**, *66*, 35–37. [[CrossRef](#)]
31. Ding, C.; Peng, H. Minimum redundancy feature selection from microarray gene expression data. *J. Bioinform. Comput. Biol.* **2005**, *3*, 185–205. [[CrossRef](#)]
32. Chawla, N.V.; Bowyer, K.W.; Hall, L.O.; Kegelmeyer, W.P. SMOTE: Synthetic minority over-sampling technique. *J. Artif. Intell. Res.* **2002**, *16*, 321–357. [[CrossRef](#)]
33. Bos, P.; van den Brekel, M.W.M.; Gouw, Z.A.R.; Al-Mamgani, A.; Waktola, S.; Aerts, H.J.W.L.; Beets-Tan, R.G.H.; Castelijns, J.A.; Jasperse, B. Clinical variables and magnetic resonance imaging-based radiomics predict human papillomavirus status of oropharyngeal cancer. *Head Neck* **2021**, *43*, 485–495. [[CrossRef](#)]

34. Ravanelli, M.; Grammatica, A.; Tononcelli, E.; Morello, R.; Leali, M.; Battocchio, S.; Agazzi, G.M.; Buglione di Monale, E.; Bastia, M.; Maroldi, R.; et al. Correlation between Human Papillomavirus Status and Quantitative MR Imaging Parameters including Diffusion-Weighted Imaging and Texture Features in Oropharyngeal Carcinoma. *AJNR. Am. J. Neuroradiol.* **2018**, *39*, 1878–1883. [[CrossRef](#)]
35. Vidiri, A.; Marzi, S.; Gangemi, E.; Benevolo, M.; Rollo, F.; Farneti, A.; Marucci, L.; Spasiano, F.; Sperati, F.; Di Giuliano, F.; et al. Intravoxel incoherent motion diffusion-weighted imaging for oropharyngeal squamous cell carcinoma: Correlation with human papillomavirus Status. *Eur. J. Radiol.* **2019**, *119*, 108640. [[CrossRef](#)]
36. Martens, R.M.; Koopman, T.; Lavini, C.; Ali, M.; Peeters, C.F.W.; Noij, D.P.; Zwezerijnen, G.; Marcus, J.T.; Vergeer, M.R.; Leemans, C.R.; et al. Multiparametric functional MRI and ¹⁸F-FDG-PET for survival prediction in patients with head and neck squamous cell carcinoma treated with (chemo)radiation. *Eur. Radiol.* **2021**, *31*, 616–628. [[CrossRef](#)]
37. de Perrot, T.; Lenoir, V.; Domingo Ayllón, M.; Dulguerov, N.; Pusztazeri, M.; Becker, M. Apparent Diffusion Coefficient Histograms of Human Papillomavirus-Positive and Human Papillomavirus-Negative Head and Neck Squamous Cell Carcinoma: Assessment of Tumor Heterogeneity and Comparison with Histopathology. *AJNR. Am. J. Neuroradiol.* **2017**, *38*, 2153–2160. [[CrossRef](#)]
38. Noij, D.P.; Martens, R.M.; Marcus, J.T.; de Bree, R.; Leemans, C.R.; Castelijns, J.A.; de Jong, M.C.; de Graaf, P. Intravoxel incoherent motion magnetic resonance imaging in head and neck cancer: A systematic review of the diagnostic and prognostic value. *Oral Oncol.* **2017**, *68*, 81–91. [[CrossRef](#)]
39. Sharma, S.J.; Wittekindt, C.; Knuth, J.; Steiner, D.; Wuerdemann, N.; Laur, M.; Kroll, T.; Wagner, S.; Klussmann, J.P. Intraindividual homogeneity of ¹⁸F-FDG PET/CT parameters in HPV-positive OPSCC. *Oral Oncol.* **2017**, *73*, 166–171. [[CrossRef](#)]
40. Moons, K.G.; Altman, D.G.; Reitsma, J.B.; Ioannidis, J.P.; Macaskill, P.; Steyerberg, E.W.; Vickers, A.J.; Ransohoff, D.F.; Collins, G.S. Transparent Reporting of a multivariable prediction model for Individual Prognosis or Diagnosis (TRIPOD): Explanation and elaboration. *Ann. Intern. Med.* **2015**, *162*, W1–W73. [[CrossRef](#)]
41. Scott-Wittenborn, N.; Fakhry, C. Epidemiology of HPV Related Malignancies. *Semin. Radiat. Oncol.* **2021**, *31*, 286–296. [[CrossRef](#)]